Wind farm density and harvested power in very large wind farms: A low-order model

G. Cortina,[1,*] V. Sharma,[2] and M. Calaf[1]
[1]*Department of Mechanical Engineering, University of Utah, Salt Lake City, Utah 84112, USA*
[2]*School of Architecture, Civil and Environmental Engineering, EPFL, Lausanne, Switzerland*
(Received 2 November 2016; published 5 July 2017)

In this work we create new understanding of wind turbine wakes recovery process as a function of wind farm density using large-eddy simulations of an atmospheric boundary layer diurnal cycle. Simulations are forced with a constant geostrophic wind and a time varying surface temperature extracted from a selected period of the Cooperative Atmospheric Surface Exchange Study field experiment. Wind turbines are represented using the actuator disk model with rotation and yaw alignment. A control volume analysis around each turbine has been used to evaluate wind turbine wake recovery and corresponding harvested power. Results confirm the existence of two dominant recovery mechanisms, advection and flux of mean kinetic energy, which are modulated by the background thermal stratification. For the low-density arrangements advection dominates, while for the highly loaded wind farms the mean kinetic energy recovers through fluxes of mean kinetic energy. For those cases in between, a smooth balance of both mechanisms exists. From the results, a low-order model for the wind farms' harvested power as a function of thermal stratification and wind farm density has been developed, which has the potential to be used as an order-of-magnitude assessment tool.

DOI: 10.1103/PhysRevFluids.2.074601

I. INTRODUCTION

Adjusting to the need of every community, the use of wind energy has been spreading around the world, either as lone standing turbines, or conforming large wind farms. Some of the advantages of installing large wind farms are the reduction in cost of energy transport, ease of connecting to the electrical grid [1], and reduced costs in land leases and permits [2], to mention a few. However, when several turbines are grouped together the corresponding turbulent wakes interact with each other [3], reducing the harvested power per wind turbine unit [4], and increasing turbines loads and fatigue [5]. Also, the capacity of the atmospheric flow to immediately recover after circulation through a succession of wind turbines is limited, and differs with atmospheric stratification [6]. Generally, the arrangement of turbines, aligned or staggered [7,8], is determined by the amount of terrain available, the local topography, and local atmospheric conditions. In either case, turbines are packed in an attempt to optimize the cost-benefit ratio.

To date, there have been many studies investigating the benefits and limitations of staggered versus aligned turbine arrangements, with results showing a dominant effect of the streamwise versus the spanwise spacing [9–11]. For example, Yang *et al.* [9] used large-eddy simulations (LESs) to evaluate the effects of turbines' spacing in very large aligned wind farms. Results demonstrated that by increasing the streamwise spacing the harvested power would increase and turbulence intensity decrease. Similarly, Meyers and Meneveau [12] used the wind farm induced surface roughness model of Calaf *et al.* [13] to investigate optimal wind turbine spacings for enhanced harvested power. Results determined that the optimal average streamwise spacing should be of the order of 15 wind turbine diameters, which is considerably higher than current spacings. In this line,

*gerard.cortina@utah.edu; http://wet.mech.utah.edu/

recent numerical simulations of finite size wind farms [11] have further demonstrated that the power output in the fully developed wind farm region depends primarily on the geometric mean turbine spacing (defined as $s = \sqrt{s_x s_y}$, where s_x and s_y indicate the streamwise and spanwise spacings, respectively), with a stronger dependence on the streamwise spacing in the aligned configurations. Additional results of Son *et al.* [14] have also demonstrated that the spacing between the first and second row of wind turbines forming a wind farm strongly affects the overall system efficiency.

An additional complexity factor is the fact that realistic atmospheric flows show significant spatiotemporal variability, hence leading to changes in an effective wind farm's arrangement. For example, recent work of Sharma *et al.* [4] illustrates that under neutral and stable stratified flows, wind turbines are well aligned as a result of a uniform mean flow direction. However, during convective regimes turbines often reorientate according to the variable local wind vector. Therefore, determining an utmost convenient wind farm arrangement remains a very complex task. To facilitate deeper understanding in this matter, a diverse set of numerical and experimental studies were developed in the past. Some examples are the works of Hansen *et al.* [15], Fitch *et al.* [16], Zhang *et al.* [17], Abkar and Porté-Agel [18,19], Peña and Rathmann [20], Peña *et al.* [21,22], Bhaganagar and Debnath [23,24], Abkar *et al.* [25], El-Askary *et al.* [26], and Stevens and Meneveau [27]. For instance, results from Peña *et al.* [21] showed that under a stable stratified Atmospheric Boundary Layer (ABL) the power deficit is a maximum, while under convective conditions the power deficit is a minimum. In this regard, Abkar and Porté-Agel [19] and Cortina *et al.* [6] reported how the extent and shape of the turbines' wakes change as a function of the background atmospheric stratification, showing that atmospheric stability has a significant effect on the spatial distribution of the mean velocity deficit and turbulence statistics in the wake region, as well as in the wake meandering characteristics. For example, under convective conditions the enhanced turbulence associated with positive buoyancy leads to a relatively larger flow entrainment and a faster wake recovery; contrarily, during stable stratified periods, wakes extend longer. It has also been illustrated that wake meandering is stronger under convective regimes, compared to neutral and stable stratified cases. These findings have also been verified with experimental data from the Horns Rev wind farm [15,22,28]. At present, several optimization and control approaches are being developed to increase the number of turbines per unit area, while reducing the corresponding turbine wakes' interactions. One of these techniques consists of using upstream scanning wind lidars to timely learn about the incoming wind conditions [29–36] and purposely misalign the wind turbine with the incoming wind, steering the wake to favorably reduce interactions with downstream turbines [37–39].

Within this work we aim to create knowledge on the wake recovery processes as a function of wind farm density, regardless of turbine arrangement. We claim that by better understanding the intervening wake recovery mechanisms it will be possible to develop more efficient wind farms, with increased harvested power per turbine unit. Earlier works on very large wind farms [11–13,40,41] have shown by means of spatiotemporal averaged quantities over the full wind farm that the recovery of the wind turbine's wake is mainly due to the vertical flux of mean kinetic energy (MKE). In this regard, the work of Stevens *et al.* [11] showed that the turbines' power output is well correlated with the vertical flux of MKE. They further demonstrated that the vertical flux of MKE is more localized along turbine columns in aligned farm arrangements than in staggered ones, leading to faster wake recoveries. Differently, in this study, we aim to examine the wake recovery process as a function of wind farm density using a local approach. For this purpose, a detailed MKE budget analysis is performed following the procedure presented by Cortina *et al.* [6]. From this analysis, a low-order model is developed that determines the harvested power of the wind turbines as a function of the wind farm density and atmospheric stability.

In Sec. II, a brief description of the wind farm numerical simulations is provided. Section III describes the distinct study cases and Sec. IV presents the mean kinetic energy budget analysis. In Sec. V, the low-order model is developed, where results are tested against the numerical data. Finally, in Sec. VI a sensitive analysis for error propagation is presented to illustrate the robustness of the low-order model. Conclusions are presented in Sec. VII.

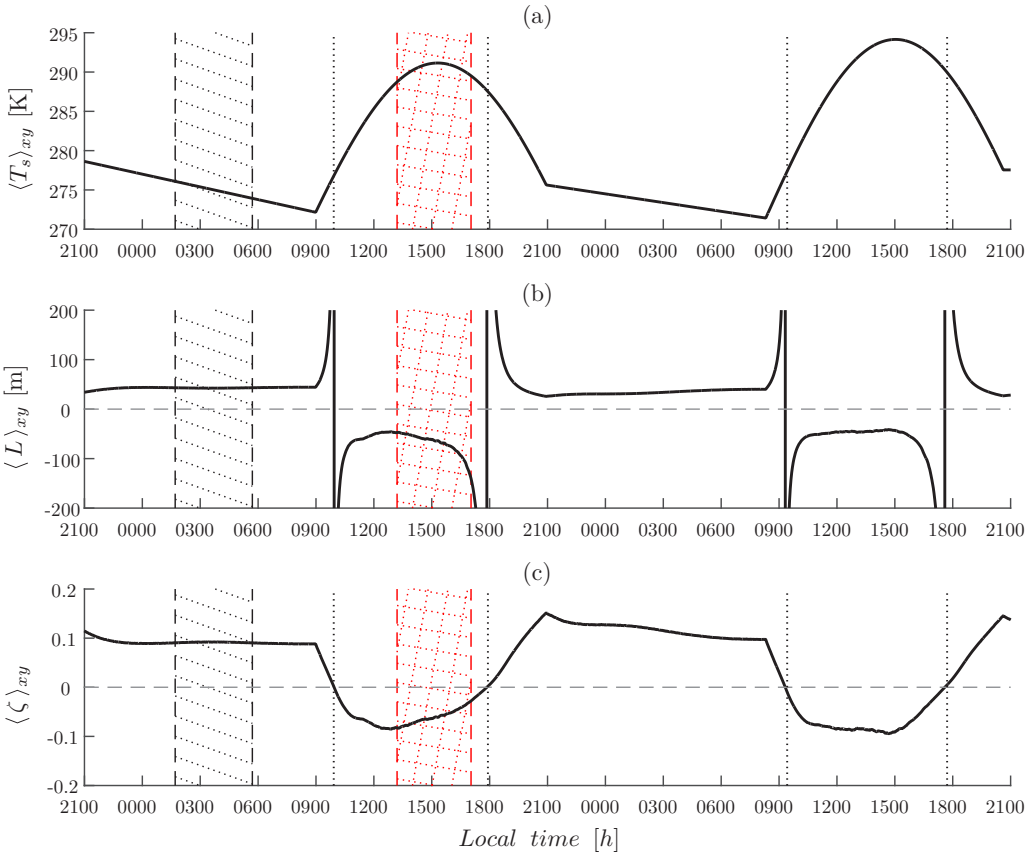

FIG. 1. (a) Spatially averaged and time-dependent imposed temperature at the surface of the domain, $\langle T_s \rangle_{xy}$, in kelvin during the evolution of two consecutive diurnal cycles; (b) the Monin-Obukhov length, $\langle L \rangle_{xy}$, in meters; and (c) the normalized stability parameter, $\langle \zeta \rangle_{xy} = z_1/\langle L \rangle_{xy}$, where z_1 is the height of the LES first grid point. The lateral brackets denote the planar average operation in the streamwise and spanwise directions. Two different periods marked with 45° dotted lines, in black, and squared dotted lines, in red, delineate time periods in which representative statistics are computed. Precisely, the first time period constitutes times between 01:45 and 05:45 local time and the second period denotes the time between 13:15 and 17:15 local time. The vertical dotted lines denote the change in stability, i.e., when $\langle \zeta \rangle_{xy} = 0$ or when $\langle L \rangle_{xy} \to \infty$. In (b) and (c) the horizontal dashed line depicts the zero value as a reference point.

II. LARGE-EDDY SIMULATION FRAMEWORK

The numerical code integrates the nondimensional and filtered Navier-Stokes equations, together with conservation of mass and an advection-diffusion equation for temperature using an LES approach. In this numerical framework, the thermal effects are coupled to the momentum equations using the Boussinesq approximation [42]. As is traditional in LES, only the energy-containing turbulent eddies are numerically resolved, and the effect of the smaller eddies is parametrized through a subgrid-scale model. The flow is forced using a time-constant and height-independent geostrophic wind equal to $(u_G, v_G) = (9, -3)\,\mathrm{ms}^{-1}$, together with a time varying surface temperature, represented in Fig. 1(a) for the evolution of two consecutive diurnal cycles. The surface temperature variation allows representation of a realistic diurnal cycle and corresponds to the experimental data set of the Cooperative Atmospheric Surface Exchange Study (CASES-99) field experiment [43]. This specific numerical simulation has been already used in other wind energy studies [4,6,16,35,36],

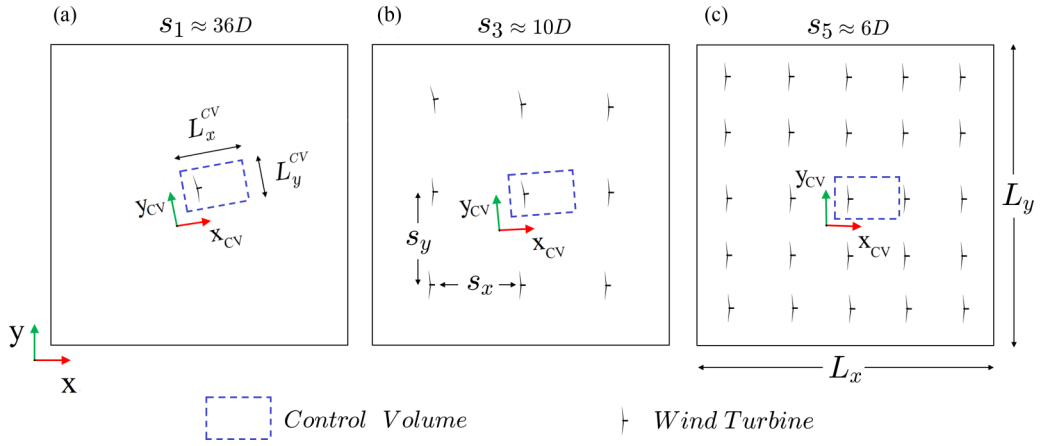

FIG. 2. (a) Case s_1, representative of 1 wind turbine located at the center of the LES domain; (b) case s_3 with a total of 9 wind turbines; and (c) case s_5 with a total of 25 wind turbines.

and for this reason it is also used here. During the evolution of this specific diurnal cycle, the ABL flow dynamically changes the thermal stratification as it transitions from nighttime to daytime, with neutral conditions being quite ephemeral. Consequently, an additional LES is considered to compute statistics under a neutral ABL stratification. For the neutral stratification, the flow is forced with the exact same geostrophic wind as the diurnal cycle, but with a constant surface temperature and a well-mixed vertical temperature profile. For all cases, the numerical domain has a lateral size equal to $L_x = L_y = \pi$ km, and a height of $z = 2$ km (see Fig. 2), and it is discretized by a total of $128\times128\times256$ grid points. As a result, the numerical resolution is 24.5 m in the streamwise and spanwise directions, and 7.8 m in the vertical direction. A pseudospectral approach is used to integrate the LES governing equations in the horizontal directions and, therefore, the numerical domain is periodic in the streamwise and spanwise directions. The initial height of the boundary layer top (z_i) is 1000 m, from which an inversion layer spans to the top of the numerical domain. In this study, the wind turbines are modeled using the actuator disk model with rotation and dynamic yaw alignment of Sharma *et al.* [44], with a yaw-readjustment time of 10 min [35,36]. The wind turbine diameter (D) is set to 100 m as well as the turbine's hub height. For further details on the numerical framework see Ref. [4].

III. STUDY CASES: WIND FARM ARRANGEMENT

To develop this study, a suite of two 4-h periods from the first diurnal cycle are selected (see Fig. 1). These two 4-h study periods are representative of two different characteristic ABL stratification regimes (unstable and stable), and because neutral stratifications are ephemeral during the evolution of the two diurnal cycles, a 4-h period is also selected from an independent LES study with a conventional neutrally stratified flow. The unstable and stable stratified periods are marked in Fig. 1 with black and red shadings for the stable and unstable regimes, respectively. Specifically, the selected stable period extends between 01:45 and 05:45, and the unstable period between 13:15 and 17:15, local time. For each stratification case, seven different wind farm arrangements have been considered to be representative of different wind farm densities, adding to a total of 21 study cases. Table I summarizes the distinct wind farm configurations, where study cases are referred as s_i, with i running from 1 to 7. In all cases, wind turbines' spacing is equidistant in both directions, streamwise and spanwise. This is illustrated in Figs. 2(a)–2(c) for cases s_1, s_3, and s_5, respectively. Each panel represents a different study case, with the corresponding LES domain and the corresponding number of turbines for that specific case. Note that because a pseudospectral approach is used to integrate the LES equations in the horizontal directions, the numerical domain is periodic in the streamwise

TABLE I. Summary of the different LES study cases for the different wind farm configurations from low (case s_1) to high (case s_7) wind farm density. The geometric mean turbine spacing is denoted by s, where $s = \sqrt{s_x s_y}$ with s_x denoting the streamwise and s_y denoting the spanwise spacing between turbines. The wind farm density is denoted by ρ_{wf}, in units of number of turbines per unit area in square kilometers.

Study case	No. of turbines	$s = \sqrt{s_x s_y}$	ρ_{wf} (no. of turbines/km^2)
s_1	1 (1×1)	$31D$	0.1
s_2	4 (2×2)	$16D$	0.5
s_3	9 (3×3)	$10D$	1.0
s_4	16 (4×4)	$8D$	1.5
s_5	25 (5×5)	$6D$	2.5
s_6	36 (6×6)	$5D$	3.5
s_7	49 (7×7)	$4.5D$	5.0

and spanwise directions and hence all wind farm configurations are in practice of infinite extent. However, also note that not in all cases does the turbulent flow reach a fully developed regime within the wind farm area. Specifically, in case s_1 turbines are spaced $31D$ apart and hence turbine-wake interactions are nonexistent and the turbulent flow does not reach a fully developed state leading to the so-called wind turbine array boundary layer limit (WTABL [13]). Contrarily, cases s_3 to s_7 present successive wind turbine–wake interactions and the turbulent flow becomes fully developed. Furthermore, depending on the ABL background stratification, case s_2 can be categorized as a stand-alone wind turbine (for unstable and neutral regimes), or as a very large wind farm (for stable regimes), where turbines are immersed in upstream turbine wakes.

Examples of the numerical domain configuration are presented in Fig. 2 for cases s_1, s_3, and s_5. In Fig. 2 the dashed blue box surrounding a wind turbine represents the control volume (CV) used to compute the local MKE budget. Note that each wind turbine of a given wind farm configuration is surrounded by a CV and statistics are averaged over all CVs of the same study case to extract a characteristic flow behavior. The CV has a streamwise distance (L_x^{CV}) that extends between a distance of $2D$ upstream of the wind turbine, down to a downstream distance where the turbine's velocity deficit recovers by 60%. The spanwise distance of the control volume is set to $L_y^{\mathrm{CV}} = 5D$, and the vertical dimension is set to $L_z^{\mathrm{CV}} = 2D$. For further details on the numerical algorithm used to compute the statistics within the local reference frame of the CV, see Ref. [6]. Cases are set such that case s_1 is representative of an isolated wind turbine, a result of the very large spacing between turbines, and it is used as reference in the following sections. On the other end of the spectrum, case s_7 corresponds to an extremely loaded case, with $s_x = s_y \approx 4.5D$.

IV. RESULTS

A. Wind farm density-dependent flow statistics

Figure 3 illustrates vertical slices of MKE for cases s_1, s_3, and s_5 under unstable, neutral, and stable atmospheric stratification. The MKE is computed as $K = \frac{1}{2}\overline{U_i}^2 = \frac{1}{2}(\overline{U}^2 + \overline{V}^2 + \overline{W}^2)$, with variables U, V, and W being the streamwise, spanwise, and vertical components of the wind vector, respectively. Statistics for the MKE are averaged over 4 h, and results are normalized with the square of the forcing geostrophic velocity.

From these vertical slices, two main characteristics are observed: (1) the MKE deficit increases with increasing wind farm density and (2) there is an increase in the length of the wind turbine wake with increasing thermal stability. From these results it is clear that the increased turbulent mixing during the unstable regime benefits wind turbine wake recovery, hence resulting in an overall smaller turbine footprint. Under neutral conditions thermally driven mixing is reduced and therefore there is a reduced recovery rate of the wind turbine wake. Finally, during the stable stratified case

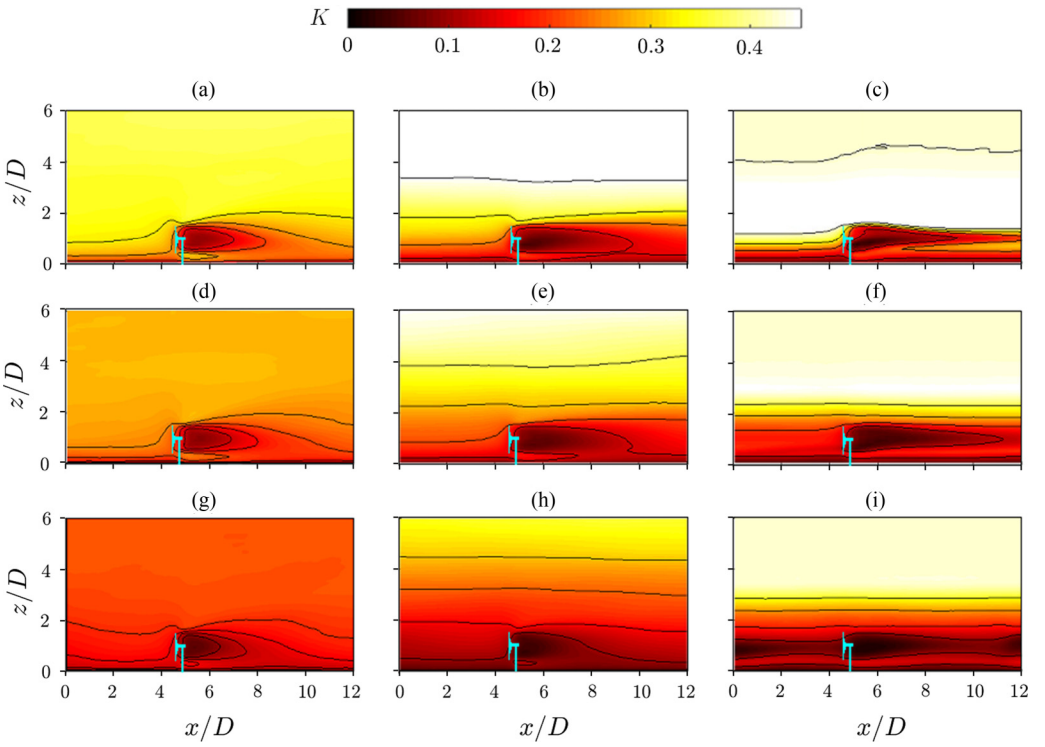

FIG. 3. Vertical slices of mean kinetic energy (K) normalized by the square of the geostrophic wind: (a), (d), (g) unstable stratified case, (b), (e), (h) neutral stratified case, and (c), (f), (i) stable stratified case. The first row (a)–(c) represents case s_1, the second row (d)–(f) represents case s_3, and the third row (g)–(i) represents case s_5.

the background turbulence is strongly attenuated and hence wakes persist for longer distances. These characteristic trends had already been observed in other earlier works [6,19,26,45–48]. Note for example the successive wake-turbine interactions illustrated in case s_5 under stable conditions [see Fig. 3(i)]. For the unstable case, it can be observed that the wake has a weak upward vertical displacement with downstream distance, with case s_1 showing the largest vertical displacement. This trend seems to weaken with increasing wind farm density. Contrarily, during the neutral regime turbine wakes seem to illustrate a weak downward vertical shift. It is also interesting to note the asymmetry of the wake during the stable period, being more intense at the top of the rotor disk and weaker near the ground. Interestingly, for the lightly loaded wind farm scenario, the wake deficit is mainly concentrated on the top half of the rotor-disk region, with a much faster wake recovery in the lower rotor-disk region. Another important result previously observed is the vertical shift of the low-level jet (LLJ) [4,16]. The LLJ is initially located at a height between 150 and 200 m for the s_1 case, and it is vertically displaced with increasing wind farm density, reaching a height of 200 and 300 m for cases s_3 and s_5, respectively. This vertical shift of the LLJ is also clearly detected in Fig. 4(c), where vertical profiles of MKE for all different study cases are presented. Note for example a vertical displacement of up to 200 m between cases s_1 and s_7. Overall, between cases s_2 and s_3, the vertical displacement is 50 m, thereby becoming much more reduced, reaching a certain stagnation between cases s_6 and s_7. A similar trend is observed for the MKE deficit in the wake region, specially at hub height. From the vertical profiles of MKE it is also interesting to note how the MKE deficit propagates vertically for the different wind farm cases. It is clear from the profiles in Fig. 4(a) that the influence of the wind farm propagates vertically up to the top of the boundary layer

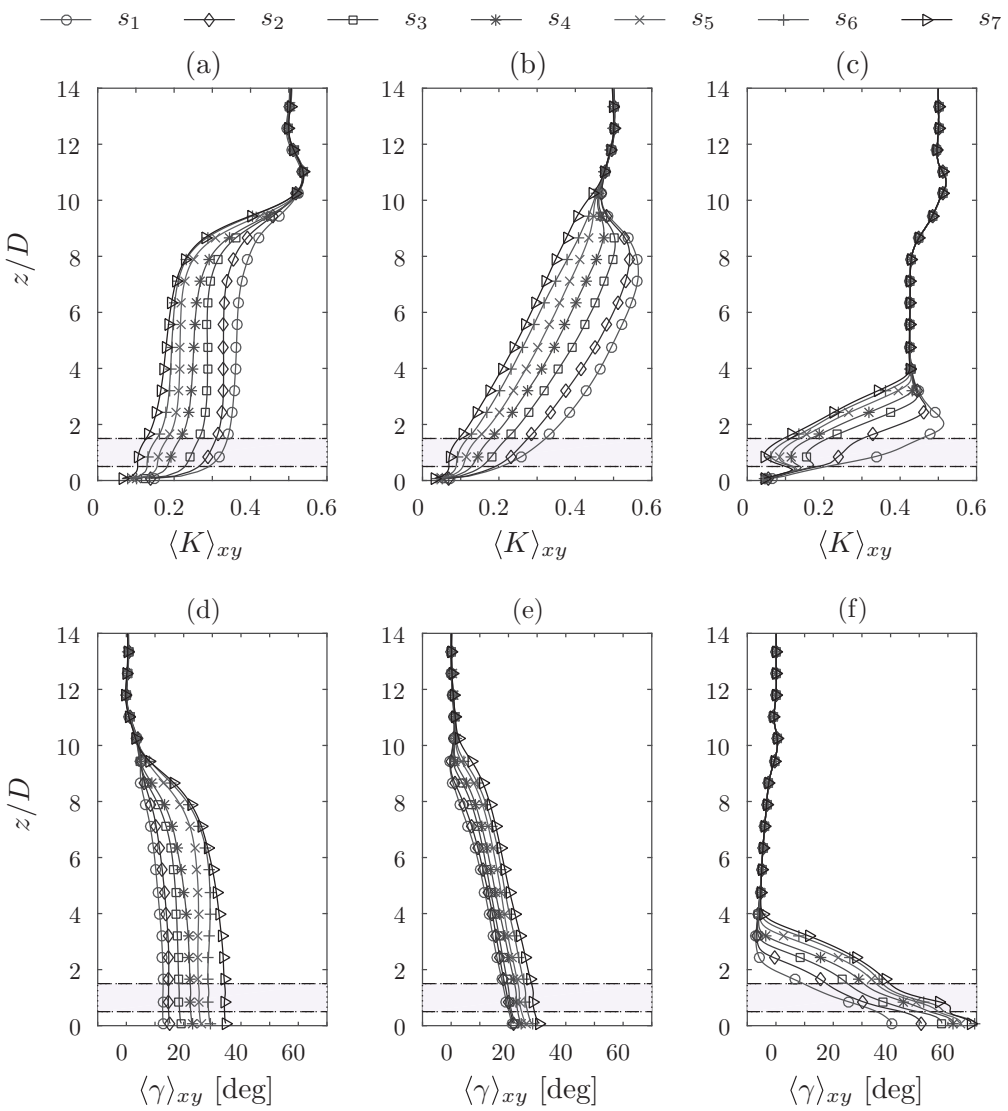

FIG. 4. The first row illustrates vertical profiles of MKE upon horizontal averaging over the LES domain, $\langle K \rangle_{xy}$, and normalized by the square of the geostrophic wind. The different lines represent results for the different wind farm density cases. Each thermal stratified regime is represented in a different column: (a) unstable, (b) neutral, and (c) stable. The bottom row represents vertical profiles of the wind veer ($\langle \gamma \rangle_{xy}$). The shaded area indicates the wind turbine rotor disk region, which ranges between $z = 0.5D$ and $z = 1.5D$.

(BL), hence affecting the entire ABL flow. For this study case, the imposed thermal inversion at the top of the BL is quite strong (3 K/100 m), and hence all cases seem to affect equally the entrainment region, regardless of wind farm loading. For the neutral case [see Fig. 4(b)], the MKE deficit follows a quasilinear profile as a function of height, with a proportional attenuation with increasing wind farm loading. In Fig. 4, we also illustrate the vertical profiles of wind veer [Figs. 4(d)–4(f)], which represent the rotation of the mean wind vector with height, related to the change in Coriolis balance as a result of the increase in wind farm loading. This is computed as $\langle \gamma \rangle_{xy} = \langle \tan^{-1}(\overline{V}/\overline{U}) \rangle_{xy}$, where $\overline{V}$ and $\overline{U}$ are the time-averaged spanwise and streamwise velocity components, respectively. The

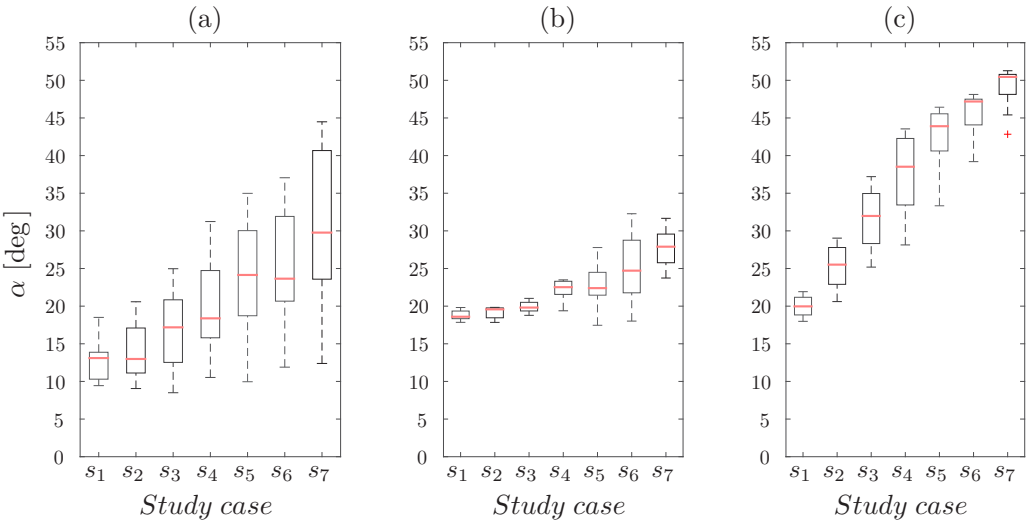

FIG. 5. Box plot based on a normal distribution of the wind turbines' yaw orientation for the different wind farm densities (from s_1 to s_7) and as a function of the atmospheric stability: (a) unstable, (b) neutral, and (c) stable.

lateral brackets denote horizontal averages over the LES domain. For all stratification cases, results illustrate an increase in wind veer with increasing wind farm loading, with a shift of $\sim 17^\circ$, 10°, and 30° between cases s_1 and s_7 for the unstable, neutral, and stable stratification regimes. The large increase during the stable regime is due to the fact that in this case most of the turbulent mixing occurring within the ABL is solely due to the wind turbines; hence the turbines' effect on the ABL is directly proportional to the wind farm density. For the unstable period, where the turbulent mixing is dominated by the convective eddies, the change in wind veer is reduced with an overall difference of 17°. Most important, however, is to note the vertical gradient in the wind veer through the rotor-disk region. This is very strong during the stable regime ($24^\circ/100$ m), much reduced during the neutral regime ($2.25^\circ/100$ m), and negligible during the unstable regime. This gradient in vertical veer induces strong loads on the wind turbine blades and towers and must be studied with care when assessing potential wind farm sites.

As mentioned earlier in Sec. II, the wind turbine model used in this work has the capacity to realign with the incoming wind vector, continuously correcting for the misalignment of the turbine's rotor disk with the incoming mean wind vector. Figure 5 illustrates the median of the turbine's yaw orientation for the different study cases together with the 25th and 75th percentiles of the yaw alignment. The distance between the top and bottom of the boxes is defined as the interquartile range, and the line in the middle of the box, represented in red, is the median of the yaw alignments. Note that in those cases where the median is not centered, it indicates a skewed distribution. Furthermore, the whiskers represent the furthest observations within the data. Finally, the outliers, marked with a red plus sign (+), display a value that is more than 1.5 times the interquartile range from the top or bottom of the box plot. From Fig. 5 it can be observed that the range of yaw alignments follows the wind veer values at the rotor-disk region illustrated earlier in Fig. 4. It is also interesting to note the increase in yaw angle with increasing wind farm loading. This progressive change in yaw angle is a result of the change in drag near the surface, affecting the geostrophic balance, and hence it is different for each stratification regime. More interesting though is the wide range in the quartiles of the yaw angle for the unstable case in comparison to the neutral and stable cases. For example, under convective conditions and for the highly loaded case s_7, the wind turbine yaw angle can change by more than 30°. This is a result of the active mixing that occurs during the convective regime. In contrast, during the neutral and stable regimes, the flow remains more steady with a reduced

requirement for the turbines to continuously readjust with the main wind. As a result, the continuous wake-to-wake interaction is very different between the different stratification regimes.

B. Mean kinetic energy budget analysis

After providing a qualitative description of the flow field for the different study cases, within this section we aim to determine the relationship between the turbines' harvested power, the atmospheric stratification, and the wind farm density. For this reason a local wind turbine MKE budget is performed for all study cases. In this respect, the corresponding MKE budget equation is written as follows:

$$\frac{\partial K}{\partial t} = -\overline{U}_j \frac{\partial K}{\partial x_j} - g\left(\frac{\overline{U}_i \overline{\theta}}{\theta_{\text{ref}}}\right)\delta_{i3} + f_c \epsilon_{ij3} \overline{U_i\, U_j} - \frac{\overline{U}_i}{\rho}\frac{\partial \overline{P}}{\partial x_i} - \frac{\partial(\overline{\tau}_{ij}\overline{U}_i)}{\partial x_j} + \overline{\tau}_{ij}\frac{\partial \overline{U}_i}{\partial x_j} + \overline{U}_i \overline{f}_i^{\text{wt}}, \quad (1)$$

where K represents the MKE, $K = \frac{1}{2}\overline{U}_i^2 = \frac{1}{2}(\overline{U}^2 + \overline{V}^2 + \overline{W}^2)$, with $\overline{U}$, $\overline{V}$, and $\overline{W}$ being the streamwise, lateral, and vertical mean velocities, respectively, with the overbar denoting the time averaging operation (i.e., for the 4-h study periods; see Fig. 1). The mean pressure is given by $\overline{P}$, and $\overline{f}_i^{\text{wt}}$ represents the force imparted on the flow by the wind turbines. The gravitational constant is denoted by g, $\overline{\theta}$ is the mean temperature, and θ_{ref} is a reference temperature. The Coriolis parameter is denoted by f_c, and ϵ_{ij3} is the alternating unit tensor ($\epsilon_{ij3} = 0$ if $i = j$, and ± 1 otherwise). The sum of the Reynolds and the subgrid-scale (SGS) shear stress is denoted by $\overline{\tau}_{ij}$. Therefore, from left to right the terms of this equation are the storage of MKE, $(\partial \overline{K}/\partial t)$, the advection of MKE, A, the gravitational acceleration, G_a, the energy due to the Coriolis force, C_g, the work due to the pressure gradient, P, the flux of MKE, ϕ, the dissipation of MKE, ϵ, and the power harvested by the wind turbines, P^{WT}. On one side the MKE of the flow is depleted by the turbines and turbulence dissipation, and on the other side, the MKE is replenished by the pressure gradient and the Coriolis force, and transported by the advection and the turbulent flux of MKE. In a steady-state regime, the storage term is null, $(\partial \overline{K}/\partial t = 0)$, and hence the equation can be rewritten as

$$0 = A + G_a + C_g + P + \phi + \epsilon + P^{\text{WT}}, \quad (2)$$

where each term is defined as follows:

$$A = -\overline{U}_j \frac{\partial K}{\partial x_j}, \quad G_a = -g\left(\frac{\overline{U}_i \overline{\theta}}{\theta_{\text{ref}}}\right)\delta_{i3}, \quad C_g = f_c \epsilon_{ij3}\overline{U_i\, U_j}, \quad P = -\frac{\overline{U}_i}{\rho}\frac{\partial \overline{P}}{\partial x_i},$$
$$\phi = -\frac{\partial(\overline{\tau}_{ij}\overline{U}_i)}{\partial x_j}, \quad \epsilon = \overline{\tau}_{ij}\frac{\partial \overline{U}_i}{\partial x_j}, \quad P^{\text{WT}} = \overline{U}_i \overline{f}_i^{\text{wt}}, \quad (3)$$

with $\overline{\tau}_{ij} = \overline{u_i' u_j'} + \overline{\tau}_{ij}^{\text{SGS}}$ being the sum of the Reynolds and the subgrid-scale shear stress.

1. *Wind farm effective power and wind turbine efficiency*

In the analysis of the different terms, we first focus on the turbine's harvested power ($P^{\text{WT}} = \overline{U}_i \overline{f}_i^{\text{WT}}$). For this purpose, Figs. 6(a) and 6(b) illustrate the wind farm effective power, EP, and the turbine's characteristic efficiency, η_{WT}, defined as

$$EP = \frac{\sum_{i=1}^{N} P_i^{\text{WT}}}{P_{s_1}^{\text{WT}}} \quad \text{and} \quad \eta_{\text{WT}} = \frac{\sum_{i=1}^{N} P_i^{\text{WT}}}{P_{s_1}^{\text{WT}}\, N}. \quad (4)$$

In Eqs. (4), N is the total number of turbines per study case (see Table I), P_i^{WT} denotes the power extracted by the turbines, and $P_{s_1}^{\text{WT}}$ is the corresponding power extracted by case s_1, which is used as a reference for normalization. This last one ($P_{s_1}^{\text{WT}}$) represents the maximum power harvested by a single wind turbine given the forcing conditions. The wind farm EP is a measure of efficiency as a function of wind farm density, illustrating how much power can be extracted by a given wind farm

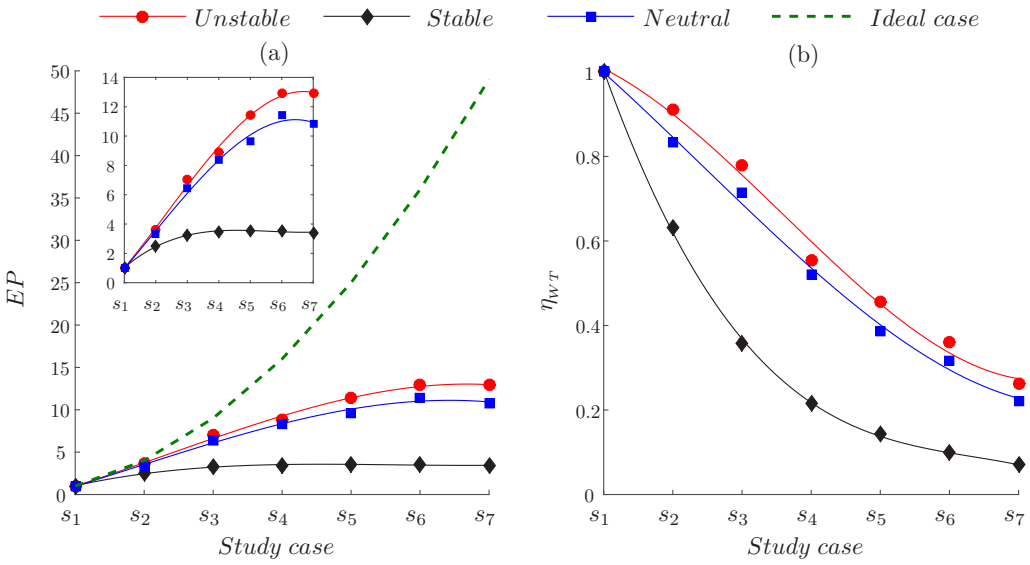

FIG. 6. (a) Effective power (EP) extracted by the wind turbines as a function of the wind farm density. (b) Characteristic efficiency of a wind turbine (η_{WT}) as a function of the wind farm density.

arrangement. For an idealized scenario EP should follow the dashed line represented in Fig. 6(a). Alternatively, the turbine's efficiency (η_{WT}) is a measure of the actual turbines' capacity to effectively harvest wind power, also as a function of farm arrangement. For an ideal case, this variable should be equal to 1, regardless of wind farm density and stratification. In Figs. 6(a) and 6(b) it can be observed that the denser the wind farm is, the larger the departure from the ideal case. For example, for case s_3 the wind farm produces an $EP \approx 7$ during the unstable and neutral regimes, meaning that there is a loss of about 30% in harvested power due to the enhanced wake interactions, a result of the wind farm density. This reduction is indeed much more accentuated for the stable regime, where for the same case s_3, EP reduces to approximately 4, representing a loss of about 60% with respect to the ideal case. From the turbines' efficiency perspective (η_{WT}), a similar behavior is observed in Fig. 6(b) for the stable stratified case, where in case s_3 each turbine only harvests about 35% of what it should if no wake interactions existed. Also of interest are the trends of EP and η_{WT} with increasing farm density and changes in atmospheric stability. For the unstable and neutral stratified cases EP increases quasilinearly with number of turbines up to case s_5, and closely following the ideal case up to case s_3. Furthermore, in case s_6, EP reaches a saturation level, where, regardless of the increase in wind farm density, EP does not increase any more; it even presents a slight decrease in case s_7. For the stable regime, saturation already occurs at s_3. These results strongly suggest that for a large wind farm under stable stratification, it might be better to turn off several turbines such to enhance EP and at the same time reduce turbine structural loads. A similar trend is correspondingly observed in the turbine efficiency [see Fig. 6(b)].

Along a similar line, an earlier experimental work of Hansen *et al.* [15] provided measurements of the power deficit at the Horns Rev wind farm as a function of wind turbine row and also under different atmospheric stability conditions. Their results already showed that the power deficit is strongly dependent on the wind turbine spacing and also concluded that, with increasing turbulence intensity, power deficit would decrease. In their work, the power deficit was presented for four different wind turbine spacings ($7D$, $9.4D$, $10.4D$, and $>20D$) and two different atmospheric stratification regimes. Results for the $10.4D$ turbine spacing case, which correlate well with the s_3 case, showed power deficit values (η_{WT}) of $\sim$0.40 and $\sim$0.70 for the stable and unstable cases, respectively. These results correspond well with the numerical results presented in Fig. 6(b): $\sim$0.37

and ∼0.71, respectively. Also, the $20D$ spacing case, corresponding to an intermediate spacing between cases s_1 and s_2, shows good correspondence, with wind turbine efficiencies ∼0.6 in Hansen *et al.*'s [15] work, and ∼0.63 in the results presented in Fig. 6(b). Finally, for the turbine spacing of $7D$, corresponding to a spacing between cases s_4 and s_5, Fig. 6(b) results overlap well with Hansen *et al.*'s data when accounting for the measured standard deviation. Therefore, it can be concluded that the numerical results approximate well the experimental data. Discrepancies could potentially arise due to the fact that the power deficit in Hansen *et al.*'s [15] work is computed by using the rated power of the wind turbines, contrary to the present analysis where turbine efficiency is derived from the power harvested from the mean flow, and in both cases the average wind velocity is below the rated wind speed. For a more thorough comparison power data should be corrected by using the corresponding turbine power coefficient. Discrepancies could also arise from the large wind farm approximation versus the finite size wind farm case of Hansen *et al.*'s [15] work.

2. MKE budget terms as a function of the wind farm density

This section provides a deeper insight into the other terms of the MKE budget. In this regard, Fig. 7 illustrates the contribution of the different MKE budget terms integrated over the streamwise and spanwise directions of the CV, and averaged over all the turbines of a given wind farm case (i.e., averaged over all the CVs, where the number of CVs is the same as the number of wind turbines for a given case). Notice that the CV approach is fundamental to unveil the corresponding MKE budget terms' behavior for the weakly loaded wind farm cases. Also, it should be noticed that in this case the CV extends from the ground up to a height of $5D$, providing a measure of the MKE redistribution for a characteristic turbine within a given wind farm arrangement as a function of height. This figure illustrates the differentiated behavior in wake recovery between cases s_1, s_3, and s_5.

Whereas for case s_5 [Figs. 7(g)–7(i)] the power harvested by the turbines mainly corresponds to the remaining balance between the MKE dissipation, the turbulent flux of MKE, and the advection of MKE, for the less loaded cases the harvested power is recovered mainly through the remaining balance between MKE dissipation, advection, and pressure redistribution. For the unstable and neutral cases the MKE is mainly recovered by a combination of advection and turbulent flux of MKE [see Figs. 7(a) and 7(b)]. Furthermore, upon closer analysis of all different cases, it is observed that advection and vertical flux of MKE are the dominant terms in the recovery of the wind turbines' harvested power. This trend is maintained equally regardless of stratification, with only small changes in the actual percentages. For example, for case s_1 the advection term represents 51%, 60%, and 73% with respect to the sum of the harvested power and dissipation for the unstable, neutral, and stable regimes, respectively. The same term only represents 35%, 38%, and 9% for case s_5. In this case, however, the turbulent flux of MKE accounts for 43%, 40%, and 26%. As we increase the wind farm density, the contribution of the turbulent flux increases. For example, in case s_7 it accounts for 70%, 85%, and 50%, which is comparable to the contribution of advection in case s_1. Therefore, it is easily concluded that by increasing wind farm density, recovery of MKE within the turbine region evolves from being advection dominated to being vertical flux dominated. From these results it is also interesting to note that while the background atmospheric stratification has a strong effect on the mechanisms to recover MKE within the turbine region for the lightly loaded cases, its effect is much reduced in the more densely packed wind farms. Finally, note that for the lightly loaded scenarios, the budget has a residual of 1.6%, 2.5%, and 1.2% for the unstable, neutral, and stable regimes, respectively, while for case s_5 the residuals decrease except for the stable case, being 1.4%, 1.5%, and 6.8%, with respect to the power extracted by the wind turbines.

In view of these results, it is questioned what would be the error associated if one was only to consider the turbines' harvested power as being replenished by advection and flux of MKE ($P^{\mathrm{WT}} \approx A + \phi$). If this error was found to be small, it could lead to the development of a reduced order model to diagnose the wind farm harvested power given a certain wind farm density and atmospheric stratification. For this purpose, Fig. 8 represents the associated absolute error $\Delta e = |(A + \phi) - P^{\mathrm{WT}}|$ for each study case. This is represented as a function of the wind farm density and

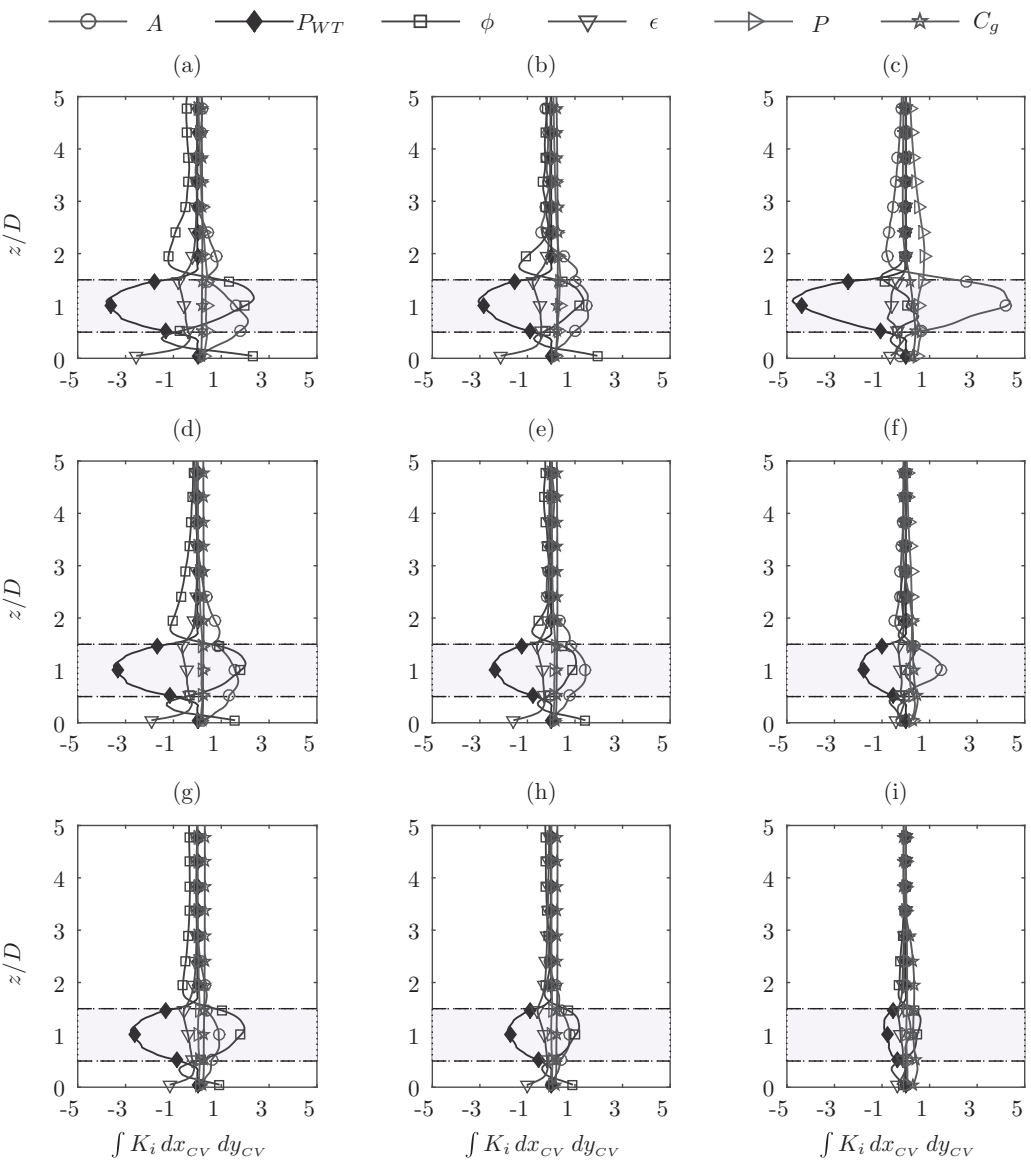

FIG. 7. Vertical profiles of the MKE budget terms (K_i), where index i denotes the different MKE budget terms: (a), (d), (g) the unstable case, (b), (e), (h) the neutral case, and (c), (f), (i) the stable regime. The first row depicts case s_1, the second row depicts case s_3, and the third row case s_5. The shaded area represents the wind turbine rotor disk from $z = 0.5D$ to $z = 1.5D$. The MKE terms are normalized by the wind turbine diameter and the cube of the geostrophic wind and, consequently, the values of the x axis should be scaled by a factor of 1×10^{-3}.

for the different atmospheric stratification conditions [unstable, neutral, and stable in Figs. 8(a), 8(b), and 8(c), respectively]. Results show small errors for the unstable and neutral cases, the largest error being equal to 0.2×10^{-3} (corresponding to a relative error of 10%), and 0.25×10^{-3} (corresponding to a relative error of 30%) for the neutral case. The stable case presents the largest errors, with a value of 0.6×10^{-3} in case s_2, corresponding to a relative error of 38%. These larger errors present in the stable case are the result of the contribution of the pressure and dissipation terms, which are

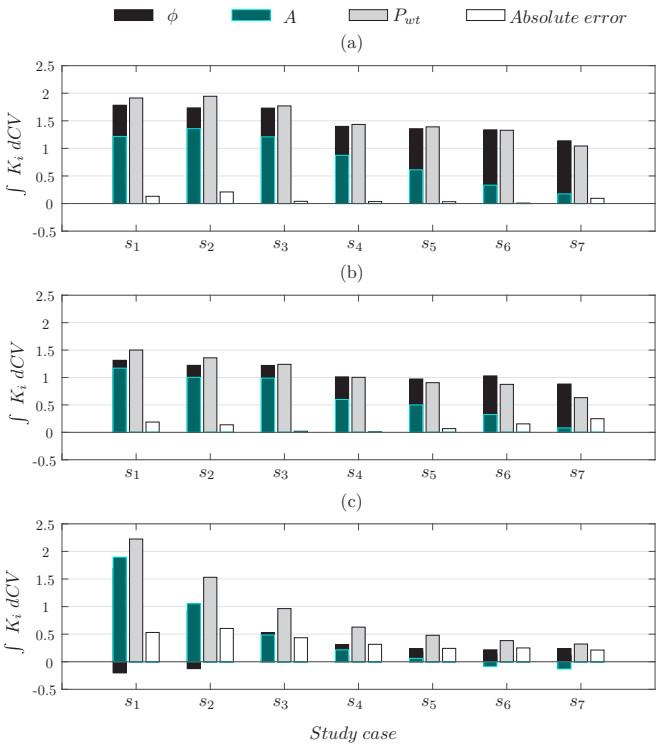

FIG. 8. Bar representation of the integration over the CV of the terms contributing to the recovery of the wind turbine power extraction (advection A and flux of MKE, ϕ, in green and black, respectively), next to the bar representation of the wind turbine power extraction (P^{WT}) in light grey. The white bar represents the absolute error $\epsilon = |(A+\phi) - P^{\mathrm{WT}}|$. (a) Unstable, (b) neutral, and (c) stable cases. The vertical axis should be scaled by a factor of 1×10^{-3}.

also important in the overall MKE budget. Despite this singular behavior of the stable case, it seems fair to assume on a first-order analysis that $P^{\mathrm{WT}} \approx A + \phi$ is a good approximation. Note that each MKE budget term depicted in Fig. 8 represents the integration of the respective term within the CV ($\int K_i\, dCV$), which now extends from $z = D/4$ to $z = 2D$ to only capture the main mechanisms that contribute to the recovery of the power extracted by the turbines.

In next section this approximation is used to develop a first order parametrization for the wind farms' harvested power as a function of the farm's density and atmospheric stratification.

V. LOW-ORDER MODEL FOR WIND FARMS' HARVESTED POWER

Upon analysis of the MKE budget presented in the previous section, as well as from earlier results [6], it seems that as a first-order approximation the wind farms' harvested power is mainly recovered through a combination of advection and flux of MKE. Therefore, one could envision an expression of the type

$$P_i \approx \lambda A_1 + (1-\lambda)\phi_N, \tag{5}$$

where P_i is the average wind turbine harvested power for any given wind farm density, i. Furthermore, A_1 is the advection term corresponding to a lone standing wind turbine (case s_1) and ϕ_N is the flux of MKE for the most intensely loaded wind farm case (s_7). In this approach, A_1 and ϕ_N represent the two most extreme values for advection and MKE flux given a geostrophic forcing. To express the

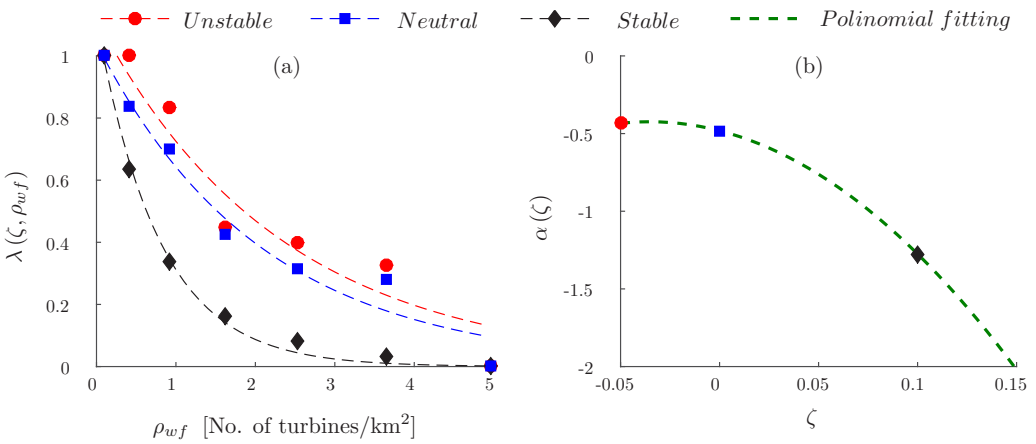

FIG. 9. (a) The weighting parameter, $\lambda(\zeta, \rho_{\mathrm{wf}})$, as a function of the wind farm density (in units of number of wind turbines per unit surface, square kilometer) for the different atmospheric stability conditions. The dashed lines are fittings of the exponential function from Eq. (7). (b) The stability correction exponent as a function of the atmospheric stability. The fitting is performed using a second-order polynomial $\alpha(\zeta) = a\zeta^2 + b\zeta + c$, with the corresponding coefficients $a = -47$, $b = -3.3$, and $c = 0.48$.

mutual relationship between the three terms (power, advection, and flux of MKE), the parameter λ is a "weighting coefficient" that redistributes the corresponding weight to either advection or flux of MKE. Hence, when $\lambda = 1$, all the harvested power is recovered through advection of MKE, and when $\lambda = 0$ the recovery occurs solely through the vertical flux of MKE. Therefore, the rate of change between the advection of MKE (A_i) and the MKE flux (ϕ_i) is determined by the weighting parameter (λ), with the assumption that both together replenish the depleted MKE ($P^{\mathrm{WT}} \approx A + \phi$). From the results, it is further evident that parameter λ should be a function of wind farm density (ρ_{wf}) and atmospheric stratification, represented here by $\zeta = z_1/\langle L \rangle_{xy}$; thus, $\lambda = \lambda(\zeta, \rho_{\mathrm{wf}})$. Therefore, Eq. (5) provides an approximate value of a turbine's harvested power (P_i) given a wind farm density and an atmospheric thermal stratification. Because, in practice, the integral of the MKE budget terms within a CV surrounding a wind turbine is not a readily available value, two additional approximations can be performed. Next, it is further assumed that all the power depleted by a stand-alone wind turbine is equal to the advection term ($P_1 \approx A_1$), and that in a highly loaded case it is equal to the vertical flux ($P_N \approx \phi_N$). As a result, Eq. (5) can be rewritten as

$$P_i \approx \lambda P_1 + (1 - \lambda) P_N. \tag{6}$$

Note that P_1 and P_N are both functions of the atmospheric stratification, $P_1(\zeta)$ and $P_N(\zeta)$. On one end P_1 can be determined by the on-site flow velocity, and P_N is the turbine power for which the EP is maximized, which in practice is equal to the wind turbine power extracted when it is located in an extremely dense wind farm scenario. Here, P_1 is the power extracted by the stand-alone wind turbine (case s_1) and P_N is the power extracted by the wind turbine from case s_7. Note that for realistic wind farm applications, the problem can be further reduced by writing P_N as a function of P_1, where P_N represents a certain percentage of P_1. In Fig. 9(a) the parameter λ is represented as a function of the wind farm density ($\rho_{\mathrm{wf}} = N/A_s$, where N is the number of wind turbines that enclose the wind farm and A_s is the surface extension of the wind farm) and for the different atmospheric stability conditions. From the numerical results an exponential fitting for λ is adjusted, represented in Fig. 9(a) by the dashed lines, and expressed as follows:

$$\lambda(\zeta, \rho_{\mathrm{wf}}) = C_o \exp(\alpha\, \rho_{\mathrm{wf}}), \tag{7}$$

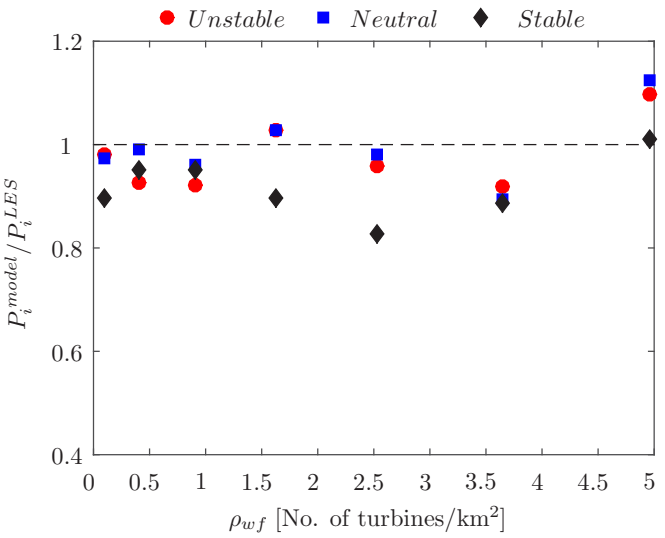

FIG. 10. Representation of the power ratio $P_i^{\text{model}}/P_i^{\text{LES}}$ as a function of the wind farm density (ρ_{wf}) in units of wind turbines per square kilometer. The variable P_i^{model} is the power obtained by the low-order model and P_i^{LES} is the power computed within the LESs; the index i denotes the different wind farm density cases (from $i = 1$ to $i = 7$).

where C_o is an adjustment coefficient and α is a stability correction exponent. In the three different fittings from Fig. 9(a), and for the sake of simplicity, C_o is taken equal to 1. The parameter α is called the stability correction exponent and it is represented in Fig. 9(b) as a function of the atmospheric stratification (ζ). It is shown that a different stability correction exponent is obtained for each corresponding stratification scenario considered. In the ideal case we could have run a larger set of stratification regimes, one could have filled additional points in Fig. 9(b). Given that this is not the case, we use the three α values we have available to fit a polynomial curve [$\alpha(\zeta) = a\zeta^2 + b\zeta + c$] that determines α as a function of the background atmospheric stratification. Because fitting a curve based on three points is far from ideal, in the next section we explore the sensitivity of hypothetical variations in α.

In summary, it can be concluded that from the curves provided in Figs. 9(a) and 9(b), it is hence possible to estimate in a first-order approximation the wind farms' harvested power given a wind farm density and given an atmospheric stability. For example, given a certain atmospheric stability, ζ, it is possible to extract the corresponding stability correction exponent, α, which in combination with ρ_{wf} provides a value for the λ parameter through Eq. (7). Next, using the parametrized power values for the two extreme cases, P_1 and P_N, in conjunction with Eq. (6), one obtains a value for the wind turbine's harvested power in a wind farm case i.

VI. ERROR ESTIMATION AND SENSITIVITY ANALYSIS FOR THE LOW-ORDER MODEL

A. Error estimation of the low-order model

In this section, the error committed when using the low-order model is evaluated by using the large-eddy simulations as a benchmark. Thus, Fig. 10 represents the power ratio $P_i^{\text{model}}/P_i^{\text{LES}}$, in the ordinate axis, and the wind farm density (ρ_{wf}) in the abscissa. The variable P_i^{model} is the power obtained by the low-order model [using Eqs. (6) and (7)] and P_i^{LES} is the power computed with the LES. The different markers denote the different atmospheric stratifications evaluated as a function of the different wind farm densities, and the horizontal solid line represents the null error with respect to the LES data.

It can be observed that the error that the model contributes varies as a function of the stability and wind farm density. On average, the overall relative error is 6%, 5%, and 8% for the unstable, neutral, and stable cases, correspondingly, where the relative error can be computed as $e = |(1 - (P_i^{\text{model}}/P_i^{\text{LES}})| \times 100)$. The maximum relative error is of the order of 10–12% for the unstable and neutral regimes, and around 17% for the stable stratified cases. Overall, the errors resultant of this parametrization are quite small, being able to predict with a good accuracy the amount of power that could be extracted from a given wind farm density under a given atmospheric stability. Again, from Fig. 10 it is demonstrated that the neutral and unstable cases have a much better predictability of the power output than the stable cases.

B. Sensitivity analysis and error propagation

In this section, and for the sake of discussion, a sensitivity analysis is performed regarding α and its effect on λ. Thus, using propagation of error theory [49], we evaluate the error committed in computing P_i given a certain uncertainty in the stability correction exponent ($\delta\alpha$). The wind turbine power uncertainty (δP_i) is based on the uncertainty in the parameter λ, which at the same time is a function of the stability correction exponent (α). Thus,

$$\delta P_i = \left.\frac{\partial \mathcal{F}_1}{\partial \lambda}\right|_{\overline{\lambda}} \delta\lambda, \tag{8}$$

where $\mathcal{F}_1 = \lambda P_1 + (1 - \lambda)P_N$, which yields the final equation for the uncertainty in the harvested power, $\delta P_i = (P_1 - P_N)\delta\lambda$. In this fashion, the associated error on λ given a small variation on alpha ($\delta\alpha$) is written as

$$\delta\lambda = \left.\frac{\partial \mathcal{F}_2}{\partial \lambda}\right|_{\overline{\alpha}} \delta\alpha. \tag{9}$$

In this expression $\mathcal{F}_2 = \exp(\alpha\rho_{\text{wf}})$, which leads to $\delta\lambda = \rho_{\text{wf}} \exp(\alpha\rho_{wf})\delta\alpha$. Finally, assuming $\delta\alpha = 10\%$, an average power error of $e_P \approx 2\%$, $\approx 3\%$, and $\approx 5\%$ will result for the unstable, neutral, and stable cases, correspondingly, where the relative uncertainty has been obtained by computing $e_P = \delta P_i/\overline{P_i}$ for the different stratifications and wind farm densities.

VII. SUMMARY AND CONCLUSIONS

This work presents an LES study of wind turbine wake recovery processes as a function of wind farm density and atmospheric stratification. For this purpose the CV approach of Cortina *et al.* [6] has been used to characterize in detail the MKE recovery processes and turbines' harvested power.

Results illustrate that the turbines' harvested power is mainly recovered by two main dominant mechanisms, advection and flux of mean kinetic energy. These two MKE recovery mechanisms are modulated by the background thermal stratification and are dependent on the wind farm density. Specifically, it has been shown that for the low-density arrangements advection dominates, while for the highly loaded wind farms the mean kinetic energy recovers through fluxes of mean kinetic energy. Of relevance from this work is the fact that for the intermediate-density cases results illustrate a smooth transition between both mechanisms. Results further illustrate that when advection dominates, the wind farm tends to be more efficient than when the MKE flux recovery dominates. Also, under stable conditions, harvested power in dense wind farms is strongly penalized due to the lack of mixing mechanisms. The results obtained on wind farm efficiency are compared with the experimental data of Hansen *et al.* [15], illustrating strong agreement.

Finally, from the LES data a low-order model for the wind farms' harvested power as a function of thermal stratification and wind farm density has been developed. This model predicts, with relatively small errors (5–15%), the power that a given wind farm under a given stability stratification could harvest. The main simplification assumption intrinsic to this model is the fact that the MKE harvested by the turbines is only recovered by advection and vertical flux. Therefore, in a first-order

approximation the contribution of the remaining MKE budget terms is neglected. Based on the experimental data, the model further assumes an equilibrium between advection and vertical flux controlled by a weighting function that depends on the wind farm density and the background thermal stratification [$\lambda = \lambda(\zeta, \rho_{wf})$], for which an experimental relationship is provided. Results show that the model works best under unstable and neutral atmospheric stratifications. Under stable regimes, the pressure distribution term also plays a relevant role in the wind turbine wakes' recovery process, hence producing larger divergences in the results from the model. This simple model has the potential to be employed as an order-of-magnitude estimation tool, which could help quickly determine the number of wind turbines that should be disconnected to optimize the harvested power provided a time changing background stratification.

ACKNOWLEDGMENTS

This research has been supported with the startup funds provided by the Mechanical Engineering Department at University of Utah to M.C. The support and resources from the Center for High Performance Computing at the University of Utah are gratefully acknowledged. V.S. thanks the support received through the Swiss National Science Foundation (Projects No. 200021134892/1 and No. 20020 125092), ETH Domain Centre for Competence in Environmental Sustainability, and the NSERC Discovery Grant (MBP) Scientific IT and Application Support (SCITAS) group at EPFL.

[1] *Renewable Energy Technologies: Cost Analysis Series* (International Renewable Energy Agency, Abu Dhabi, UAE, 2012), Vol. 1.

[2] C. Mon, T. Stehly, B. Maples, and E. Settle, 2014 cost of wind energy review, National Renewable Energy Laboratory, Report No. NREL/TP-6A20-64281, 2014.

[3] S. Rockel, J. Peinke, M. Hölling, and R. B. Cal, Wake to wake interaction of floating wind turbine models in free pitch motion: An eddy viscosity and mixing length approach, Renew. Energy **85**, 666 (2016).

[4] V. Sharma, M. B. Parlange, and M. Calaf, Perturbations to the spatial and temporal characteristics of the diurnally-varying atmospheric boundary layer due to an extensive wind farm, Boundary-Layer Meteorol. **162**, 255 (2017).

[5] S. Lee, M. Churchfield, P. Moriarty, J. Jonkman, and J. Michalakes, Atmospheric and wake turbulence impacts on wind turbine fatigue loadings, in *Proceedings of the 50th AIAA Aerospace Sciences Meeting Including the New Horizons Forum and Aerospace Exposition* (American Institute of Aeronautics and Astronautics, Reston, VA, 2012), p. 540.

[6] G. Cortina, M. Calaf, and R. B. Cal, Distribution of mean kinetic energy around an isolated wind turbine and a characteristic wind turbine of a very large wind farm, Phys. Rev. Fluids **1**, 074402 (2016).

[7] R. J. A. M. Stevens, Dependence of optimal wind turbine spacing on wind farm length, Wind Energy **19**, 651 (2016).

[8] R. J. A. M. Stevens, B. F. Hobbs, A. Ramos, and C. Meneveau, Combining economic and fluid dynamic models to determine the optimal spacing in very large wind farms, Wind Energy **20**, 465 (2017).

[9] X. Yang, S. Kang, and F. Sotiropoulos, Computational study and modeling of turbine spacing effects in infinite aligned wind farms, Phys. Fluids **24**, 115107 (2012).

[10] V. Sharma, G. Cortina, F. Margairaz, M. B. Parlange, and M. Calaf, Evolution of flow characteristics through finite-sized wind farms and influence of turbine arrangement (unpublished).

[11] R. J. Stevens, D. F. Gayme, and C. Meneveau, Effects of turbine spacing on the power output of extended wind-farms, Wind Energy **19**, 359 (2016).

[12] J. Meyers and C. Meneveau, Optimal turbine spacing in fully developed wind farm boundary layers, Wind Energy **15**, 305 (2012).

[13] M. Calaf, C. Meneveau, and J. Meyers, Large eddy simulation study of fully developed wind-turbine array boundary layers, Phys. Fluids **22**, 015110 (2010).
[14] E. Son, S. Lee, B. Hwang, and S. Lee, Characteristics of turbine spacing in a wind farm using an optimal design process, Renew. Energy **65**, 245 (2014).
[15] K. S. Hansen, R. J. Barthelmie, L. E. Jensen, and A. Sommer, The impact of turbulence intensity and atmospheric stability on power deficits due to wind turbine wakes at Horns Rev wind farm, Wind Energy **15**, 183 (2012).
[16] A. C. Fitch, J. K. Lundquist, and J. B. Olson, Mesoscale influences of wind farms throughout a diurnal cycle, Mon. Weather Rev. **141**, 2173 (2013).
[17] W. Zhang, C. D. Markfort, and F. Porté-Agel, Wind-turbine wakes in a convective boundary layer: A wind-tunnel study, Boundary-Layer Meteorol. **146**, 161 (2013).
[18] M. Abkar and F. Porté-Agel, The effect of free-atmosphere stratification on boundary-layer flow and power output from very large wind farms, Energies **6**, 2338 (2013).
[19] M. Abkar and F. Porté-Agel, Influence of atmospheric stability on wind-turbine wakes: A large-eddy simulation study, Phys. Fluids **27**, 035104 (2015).
[20] A. Peña and O. Rathmann, Atmospheric stability-dependent infinite wind-farm models and the wake-decay coefficient, Wind Energy **17**, 1269 (2014).
[21] A. Peña, P.-E. Réthoré, and O. Rathmann, Modeling large offshore wind farms under different atmospheric stability regimes with the park wake model, Renew. Energy **70**, 164 (2014), special issue on aerodynamics of offshore wind energy systems and wakes.
[22] A. Peña, P.-E. Réthoré, and M. P. van der Laan, On the application of the Jensen wake model using a turbulence-dependent wake decay coefficient: The Sexbierum case, Wind Energy **19**, 763 (2016).
[23] K. Bhaganagar and M. Debnath, Implications of stably stratified atmospheric boundary layer turbulence on the near-wake structure of wind turbines, Energies **7**, 5740 (2014).
[24] K. Bhaganagar and M. Debnath, The effects of mean atmospheric forcings of the stable atmospheric boundary layer on wind turbine wake, J. Renew. Sustainable Energy **7**, 013124 (2015).
[25] M. Abkar, A. Sharifi, and F. Porté-Agel, Wake flow in a wind farm during a diurnal cycle, J. Turbul. **17**, 420 (2016).
[26] W. El-Askary, I. Sakr, A. M. AbdelSalam, and M. Abuhegazy, Modeling of wind turbine wakes under thermally-stratified atmospheric boundary layer, J. Wind Eng. Ind. Aerodyn. **160**, 1 (2017).
[27] R. J. Stevens and C. Meneveau, Flow structure and turbulence in wind farms, Annu. Rev. Fluid Mech. **49**, 311 (2017).
[28] M. Méchali, R. Barthelmie, S. Frandsen, L. Jensen, and P.-E. Réthoré, Wake effects at Horns Rev and their influence on energy production, in *Proceedings of the European Wind Energy Conference and Exhibition* (CiteSeer, 2006).
[29] M. Harris, D. Bryce, A. Coffey, D. Smith, J. Birkemeyer, and U. Knopf, Advance measurements of gusts by laser anemometry, Wind Eng. Ind. Aerodyn. **95**, 1637 (2007).
[30] K. Kragh, M. Hansen, and T. Mikkelsen, Improving yaw alignment using spinner based lidar, in *Proceedings of 49th AIAA Aerospace Sciences Meeting Including the New Horizons Forum and Aerospace Exposition* (American Institute of Aeronautics and Astronautics, Orlando, FL, 2011), paper 2011-264.
[31] E. Simley, L. Pao, R. Frehlich, B. Jonkman, and N. Kelley, Analysis of wind speed measurements using continuous wave lidar for wind turbine control, in *Proceedings of the 49th AIAA Aerospace Sciences Meeting Including the New Horizons Forum and Aerospace Exposition* (American Institute of Aeronautics and Astronautics, Orlando, FL, 2011), paper 2011-263.
[32] G. Iungo, W. Yu-Ting, and F. Porté-Agel, Field measurements of wind turbine wakes with lidars, J. Atmos. Ocean. Technol. **30**, 274 (2012).
[33] K. Kragh and P. Fleming, Rotor speed dependent yaw control of wind turbines based on empirical data, in *Proceedings of the 50th AIAA Aerospace Sciences Meetings and Exhibit* (American Institute of Aeronautics and Astronautics, Nashville, Tennessee, 2012), paper 2012-1018.

[34] T. Mikkelsen, N. Angelou, K. Hansen, M. Sjöholm, M. Harris, C. Slinger, P. Hadley, R. Scullion, G. Ellis, and G. Vives, A spinner-integrated wind lidar for enhanced wind turbine control, Wind Energy **16**, 625 (2013).

[35] G. Cortina, V. Sharma, and M. Calaf, Investigation of the incoming wind vector for improved wind turbine yaw-adjustment under different atmospheric and wind farm conditions, Renew. Energy **101**, 376 (2017).

[36] G. Cortina and M. Calaf, Turbulence upstream of wind turbines: A large-eddy simulation approach to investigate the use of wind lidars, Renew. Energy **105**, 354 (2017).

[37] P. A. Fleming, P. M. O. Gebraad, S. Lee, J. W. van Wingerden, K. Johnson, M. Churchfield, J. Michalakes, P. Spalart, and P. Moriarty, Evaluating techniques for redirecting turbine wakes using SOWFA, Renew. Energy **70**, 211 (2014).

[38] P. M. O. Gebraad and J. W. van Wingerden, A control-oriented dynamic model for wakes in wind plants, J. Phys.: Conf. Ser. **524**, 012186 (2014).

[39] M. J. Churchfield, P. Fleming, B. Bulder, and S. M. White, Wind turbine wake-redirection control at the fishermen's atlantic city windfarm, National Renewable Energy Laboratory, Report No. NREL/CP-5000-63575, 2015.

[40] R. B. Cal, J. Lebrón, L. Castillo, H. S. Kang, and C. Meneveau, Experimental study of the horizontally averaged flow structure in a model wind-turbine array boundary layer, J. Renew. Sustainable Energy **2**, 013106 (2010).

[41] C. VerHulst and C. Meneveau, Altering kinetic energy entrainment in large eddy simulations of large wind farms using unconventional wind turbine actuator forcing, Energies **8**, 370 (2015).

[42] R. Stull, *An Introduction to Boundary Layer Meteorology*, Atmospheric Science Library (Springer, Berlin, 1988).

[43] G. S. Poulos, W. Blumen, D. C. Fritts, J. K. Lundquist, J. Sun, S. P. Burns, C. Nappo, R. Banta, R. Newsom, J. Cuxart, E. Terradellas, B. Balsley, and M. Jensen, CASES-99: A comprehensive investigation of the stable nocturnal boundary layer, Bull. Am. Meteorol. Soc. **83**, 555 (2002).

[44] V. Sharma, M. Calaf, M. Lehning, and M. B. Parlange, Time-adaptive wind turbine model for an LES framework, Wind Energy **19**, 939 (2016).

[45] M. Magnusson and A.-S. Smedman, Influence of atmospheric stability on wind turbine wakes, Wind Eng. **18**, 139 (1994).

[46] L. P. Chamorro and F. Porté-Agel, A wind-tunnel investigation of wind-turbine wakes: Boundary-layer turbulence effects, Boundary-Layer Meteorol. **132**, 129 (2009).

[47] L. P. Chamorro and F. Porté-Agel, Effects of thermal stability and incoming boundary-layer flow characteristics on wind-turbine wakes: A wind-tunnel study, Boundary-Layer Meteorol. **136**, 515 (2010).

[48] R. J. Barthelmie and L. E. Jensen, Evaluation of wind farm efficiency and wind turbine wakes at the Nysted offshore wind farm, Wind Energy **13**, 573 (2010).

[49] H. H. Ku, Notes on the use of propagation of error formulas, J. Res. Natl. Bur. Stand. Sect. C **70C**, 263 (1996).